Supporting Information

Deeply Reconstructed NiOOH/FeOOH Interface in Nanoboxes with Accelerated Kinetics for Oxygen Evolution Reaction

Ping Yan[a†], Qian Liu[b†], Hui Zhang[c*], Luchun Qiu[a], Hao Bin Wu[b*] and Xin-Yao Yu[a,d,e*]

[a]Institutes of Physical Science and Information Technology, Key Laboratory of Structure and Functional Regulation of Hybrid Materials, Anhui University, Ministry of Education, Hefei 230601, (P. R. China)

[b]School of Materials Science & Engineering, Zhejiang University, Hangzhou 310027, (P. R. China)

[c]School of Physics and Materials Science, Anhui University, Hefei 230601, (P. R. China)

[d]Anhui Graphene Engineering Laboratory, Anhui University, Hefei 230601, (P. R. China)

[e]Energy Materials and Devices Key Lab of Anhui Province for Photoelectric Conversion, Anhui University, Hefei 230601, (P. R. China)

[†]These two authors contribute equally to this work.

***Corresponding Authors**

*Email: yuxinyao@ahu.edu.cn

*Email: hbwu@zju.edu.cn

*Email: zhhui@ahu.edu.cn

Experimental

Materials

Nickel chloride hexahydrate ($NiCl_2 \cdot 6H_2O$), trisodium citrate dehydrate ($C_6H_5Na_3O_7 \cdot 2H_2O$), potassium hexacyanoferrate (III) ($K_3Fe(CN)_6$), potassium tetracyanidonickelate (II) ($K_2Ni(CN)_4$), potassium hexacyanoferrate (II) trihydrate ($K_4Fe(CN)_6 \cdot 3H_2O$), polyvinylpyrrolidone (PVP, K-30), sodium hypophosphite (NaH_2PO_2), hydrochloric acid (HCl), potassium hydroxide (KOH), and dimethylformamide (DMF) were purchased from Sinopharm Chemical Reagent Co.. Pt/C and RuO_2 commercial catalysts were purchased from Macklin. All purchased chemicals were not further purified and all solvents were analytical grade.

Synthesis of NiFe-PBA nanocubes (denoted as NiFe-PBA NCs)

A simple precipitation method was employed to prepare NiFe-PBA NCs. In a typical synthesis, 0.66 g of $C_6H_5Na_3O_7 \cdot 2H_2O$ and 0.286 g of $NiCl_2 \cdot 6H_2O$ were mixed with 40 mL of deionized water (DIW). 0.264 g of $K_3Fe(CN)_6$ was dissolved in 40 of mL of DIW. Then, the two solutions were mixed under continuous magnetic stirring. After magnetic stirring for 2 min, the obtained green solution remained stationary for a day at 25 ^oC. After that, the yellow products were centrifuged at 9000 rpm and then washed alternately with ethanol and DIW for more than three times. Finally, the precipitates were dried at 50 ^oC overnight.

Synthesis of NiNi PBA nanoplates (denoted as NiNi-PBA NPs)

In a typical synthesis, 0.16 g of $C_6H_5Na_3O_7 \cdot 2H_2O$ and 0.19 g of $NiCl_2 \cdot 6H_2O$ were were mixed with 40 mL of DIW. Then, 0.192 g of $K_2Ni(CN)_4$ was dissolved in 40 mL of DIW. The following procedures were the same as those for the synthesis of NiFe-PBA NCs.

Synthesis of Fe Prussian blue nanocubes (denoted as Fe-PB NCs)

In a typical synthesis, 3.8 g of PVP and 0.11 g of $K_4Fe(CN)_6 \cdot 3H_2O$ were dissolved in 50 mL of HCl solution (0.1 mol/L) and stirred for 30 min to form a clear yellow solution. Then, the bottle was placed into an electric oven at 80 ^oC for one day. After that, the dark blue

products were centrifuged at 9000 rpm and then washed alternately with ethanol and DIW for more than three times. Finally, the precipitates were dried at 50 ^{o}C overnight.

Synthesis of etched NiFe-PBA NCs

In a typical synthesis, 0.03 g of NiFe-PBA NCs were dispersed in 30 mL of DMF under stirring for 25 min. Then, placed the mixture in an autoclave and setted the temperature to 200 ^{o}C for different time. When the temperature was cooled to room temperature, the dark green products were centrifuged at 9000 rpm and then washed alternately with ethanol and DIW for more than three times. Finally, the precipitates were dried at 50 ^{o}C overnight. The NiFe-PBA etched in DMF for different etching time are denoted as NiFe-PBA-DMF-*n* where *n* corresponds to the etching time (5 h, 10 h, and 20 h).

Synthesis of NiFeP NBs

In a typical synthesis, 0.02 g of NiFe-PBA-DMF-20 h and 0.4 g of NaH_2PO_2 were placed on two separate ends of a porcelain boat in which NaH_2PO_2 was located at upstream of the tube furnace. Then, the phosphidation reaction occurred at 400 ^{o}C for 2 h under nitrogen atmosphere with a heating rate of 2 ^{o}C min^{-1}. When the temperature was cooled to room temperature, the NiFeP NBs were obtained.

Synthesis of porous NiFe phosphide nanocubes (denoted as NiFeP NCs), nickel phosphide nanoplates (denoted as NiP NPs), and iron phosphide nanocubes (denoted as FeP NCs)

The whole synthesis process is similar to that of NiFeP NBs, except for using NiFe-PBA NCs, NiNi-PBA NPs, and Fe-PB NCs as the precursors for further phosphorization.

Synthesis of NiFe phosphides with other Ni/Fe ratios

The whole synthesis process is similar to that of NiFe-PBA NCs, except for using 0.191 g, 0.381g and 0.475g of $NiCl_2 \cdot 6H_2O$ to synthesize NiFe-PBA-1, NiFe-PBA-2, and NiFe-PBA-3, respectively. After etching with DMF for 20 h, they are denoted as NiFe-PBA-1-DMF 20 h, NiFe-PBA-2-DMF-20 h, and NiFe-PBA-3-DMF-20 h. After phosphidation, the corresponding metal phosphides are denoted as NiFeP-1, NiFeP-2, and NiFeP-3.

Synthesis of NiFe-LDH

In a typical synthesis, 600.6 mg of urea was dissolved in 40 mL of H_2O under constant magnetic stirring in a 100 mL Teflon container. Then 814.2 mg of $Ni(NO_3)_2 \cdot 6H_2O$, 484.8 mg of $Fe(NO_3)_3 \cdot 9H_2O$ and 148.1 mg of NH_4F were added in and dissolved in the solution. After stirring for another 10 min, the container was transferred into a stainless autoclave and put in an electric oven at 120 °C for 6 h. After cooling down to the ambient temperature, the precipitates were collected by centrifugation and washed by ethanol for more than 3 times.

Material characterizations

The morphologies and elemental contents of all obtained samples were characterized by using scanning electron microscopy (SEM) instrument with energy-dispersive X-ray spectroscopy (EDS) (Zeiss sigma 500) and transmission electron microscope (TEM) instrument (FEI Tecnai G2 F20). The X-ray diffraction (XRD) studies were performed on PANalytical Empyrean. The chemical valence state of as-obtained samples were analyzed on Thermo Fischer ESCALAB 250 Xi. The *in-situ* Raman spectra were determined by Confotec™ MR 520 using a 532 nm laser with an acquisition time of 10 s. The phosphate species of metal phosphides from chemical oxidation in 1 M KOH is detected by 930 Compact ion chromatography (IC) Flex.

Electrochemical characterizations

All electrochemical tests were conducted by using CHI 760E at room temperature. 1 M KOH electrolyte was used in the experiment. Graphite rod was applyed as counter electrode and Hg/HgO electrode was employed as reference electrode. All potentials were referenced to the potentials of the reversible hydrogen electrode (RHE). To prepare the working electrode, the as-obtained powers or Pt/C and RuO_2 (5.0 mg) were dispersed in a mixed solution composed of ethanol (270 μL), H_2O (200 μL), and Nafion (5 wt%, 30 μL) solution under ultrasonicating for 50 min to come into being a uniformly dispersed ink. After that, 2.5 μL of ink was dropped onto the rotating disk electrode (RDE). The loading amount of catalysts on

RDE was 0.35 mg cm^{-2}. Finally, the RDE was dried at 25 ^{o}C for further characterization. To eliminate the resulting oxygen bubble, the RDE was rotated at 1600 rpm.

All the linear sweep voltammogram (LSV) curves of all samples were performed at 5 mV s^{-1}. All polarization curves were corrected by 95% *iR*-compensation. The double-layer capacitance (C_{dl}) method was used to estimate the electrochemical active surface area (ECSA). As for C_{dl}, it was acquired by cyclic voltammetry (CV) method at different scanning rates between 0.82 V and 0.92 V *vs*. RHE (20-120 mV s^{-1}). The differences of current densities at 0.87 V were plotted as a function of scan rates. The slope of the fitted line was equal to half of the C_{dl}. The electrochemical impedance spectroscopy (EIS) test was collected at an amplitude of 5 mV as well as frequency range of 10^5~0.1 Hz. When Ni foam is used as support, the as-obtained samples were loaded onto Ni foam. The loading amount of catalysts on Ni foam was 2 mg cm^{-2}. The stability test was performed by chronoamperometry (CA) method at a constant potential. The following formula was used to calculate the turnover frequency (TOF) values:[1]

$$TOF = \frac{I}{x \times n \times F}$$

Where I is the current at a specific overpotential and x refers to the number of electrons transfer. F represents Faraday constant (96485 C mol^{-1}). n refers to the number of moles of metal active species (including Ni and Fe).

The faradaic efficiency (FE) for OER was studied by rotating ring-disk electrode (RRDE). The generated O_2 molecules were detected by oxygen reduction reaction when the ring potential was 0.4 V. The FE value of O_2 was calculated using the following equation:[2]

$$FE(O_2) = \frac{I_{ring}}{I_{disk} \times N}$$

Where I_{ring} means the ring current. I_{disk} denotes the disk current. N represents the collection efficiency (here is 0.424).

The gas chromatography (GC-9790) was employed to measure the evolution amount of H_2 at 10 mA cm^{-2}. The following equation was used to calculate the FE of H_2:[3]

$$FE(H_2) = \frac{2 \times n \times F}{I \times t}$$

Where *n* means the molar amount of produced H_2. *I* refers to the current (A) when the HER is tested. *t* is the reaction time.

2.9 Theoretical calculations

The Vienna ab-initio simulation package (VASP) was used to calculate all the density functional theory (DFT).[4] The projector augmented-wave (PAW) potentials were employed and the plane wave basis with energy cutoff was 500 eV.[5] The generalized gradient approximation with the function of Perdew–Burke–Ernzerhof (GGA-PBE) was applied to describe the exchange–correlation function.[6] The van der Waals (vdW) interactions were described by Grimme's semiempirical DFT-D3 scheme of dispersion correction.[7] All geometric structures were fully relaxed until energy and forces were converged to 10^{-5} eV and 0.02 eV $Å^{-1}$. (101) surface of FeOOH and (101) surface of NiOOH were modelled with 20 Å vacuum. The Brillouin zone was sampled using 4 × 3 × 1 *k*-mesh for geometry optimization.[8] The Gibbs free energy differences at each step and theoretical overpotential of the OER is obtained based on Nørskov *et al*.[9]

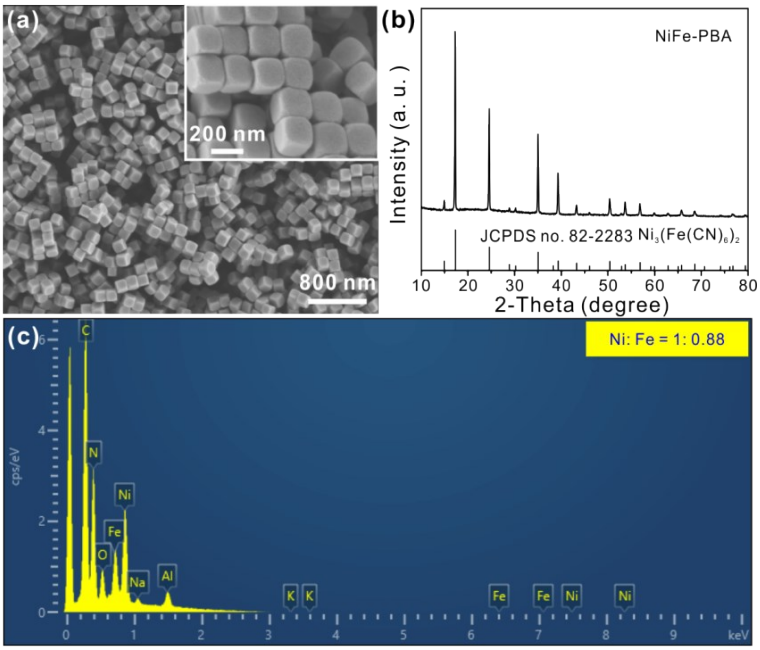

Fig. S1 (a) Large-scale SEM image, (b) XRD pattern, and (c) EDX spectrum of NiFe-PBA NCs. The inset is the high-magnification SEM image of NiFe-PBA NCs.

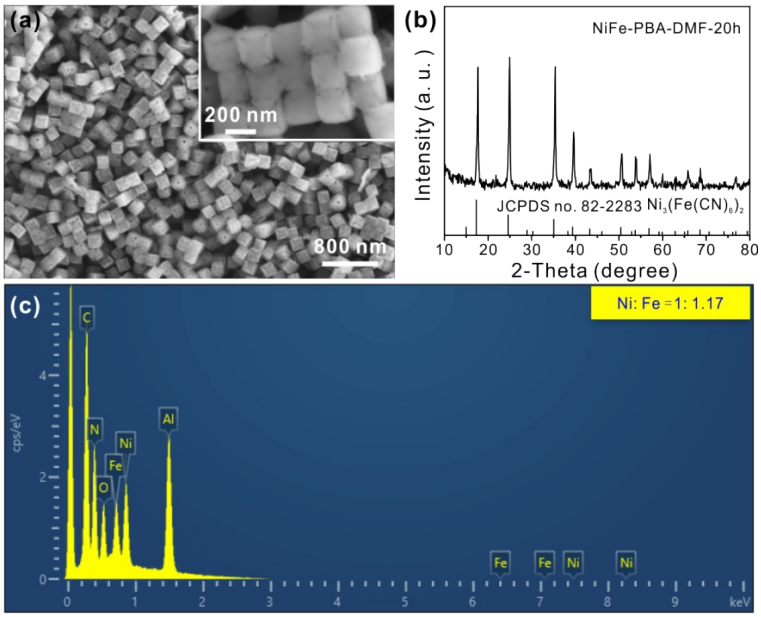

Fig. S2 (a) Large-scale SEM image, (b) XRD pattern, and (c) EDX spectrum of NiFe-PBA-DMF-20 h. The inset is the high-magnification SEM image of NiFe-PBA-DMF-20 h.

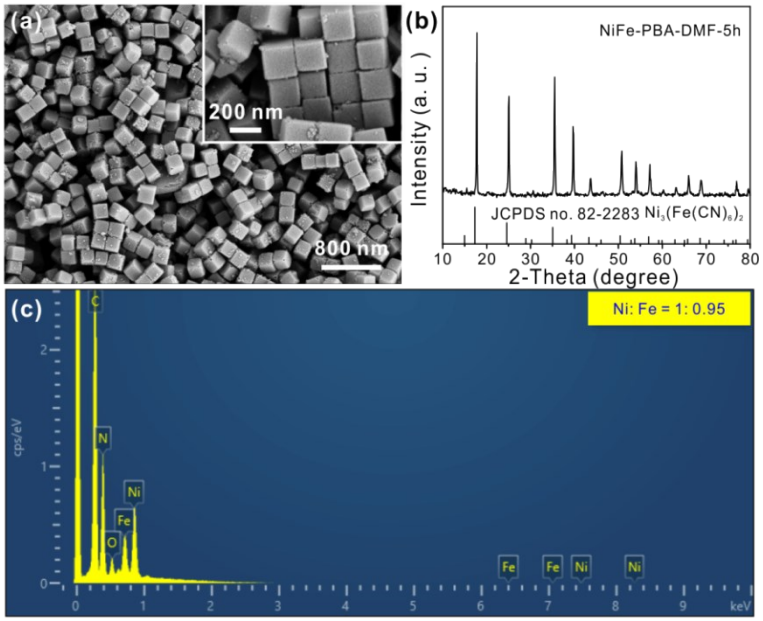

Fig. S3 (a) Large-scale SEM image, (b) XRD pattern, and (c) EDX spectrum of NiFe-PBA-DMF-5 h. The inset is the high-magnification SEM image of NiFe-PBA-DMF-5 h.

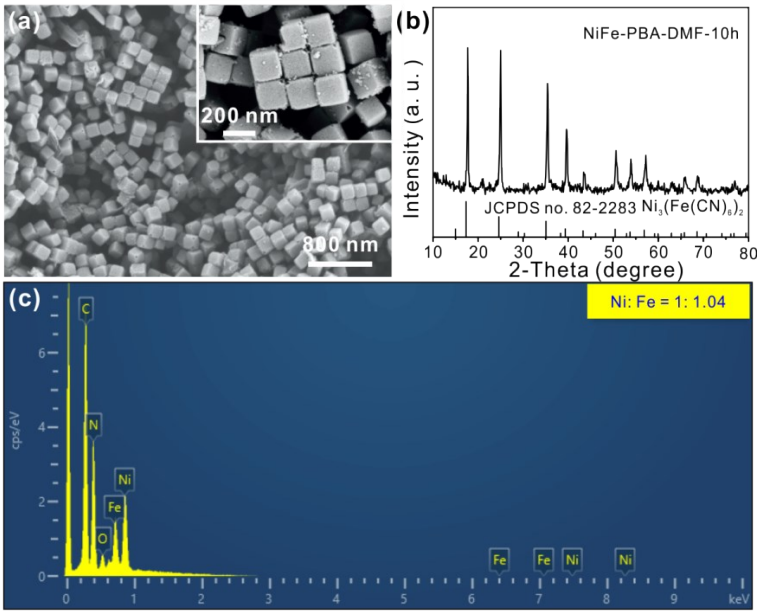

Fig. S4 (a) Large-scale SEM image, (b) XRD pattern, and (c) EDX spectrum of NiFe-PBA-DMF-10 h. The inset is the high-magnification SEM image of NiFe-PBA-DMF-10 h.

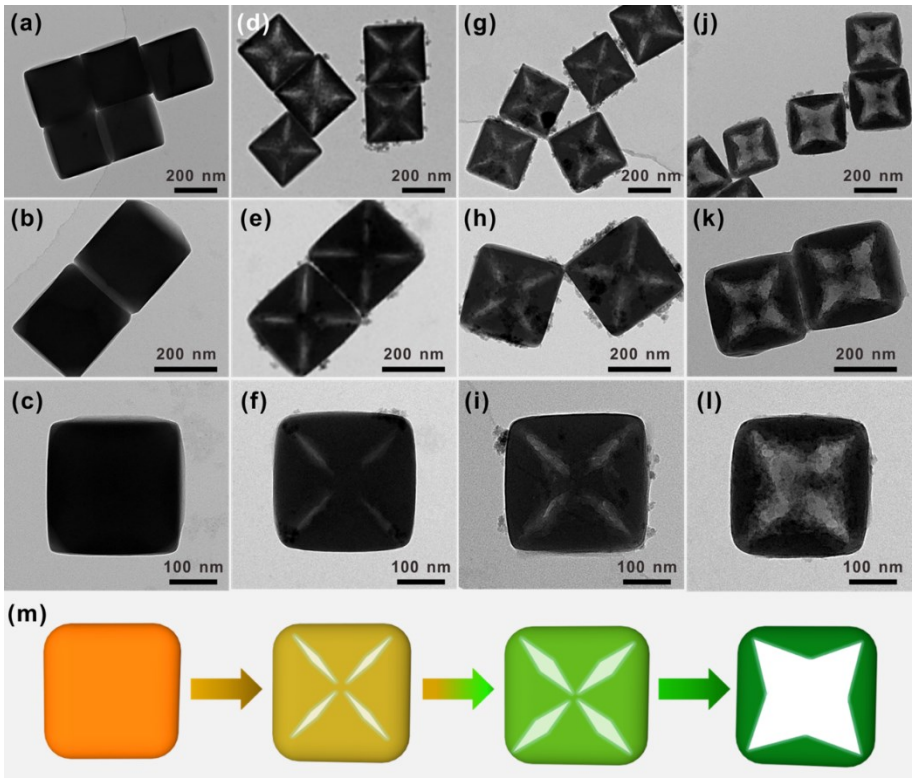

Fig. S5 (a–l) TEM images of the samples in the etching procedure at 0 h (a-c), 5 h (d-f), 10 h (g-i), and 20 h (j-l). (m) Schematic illustration for the etching process.

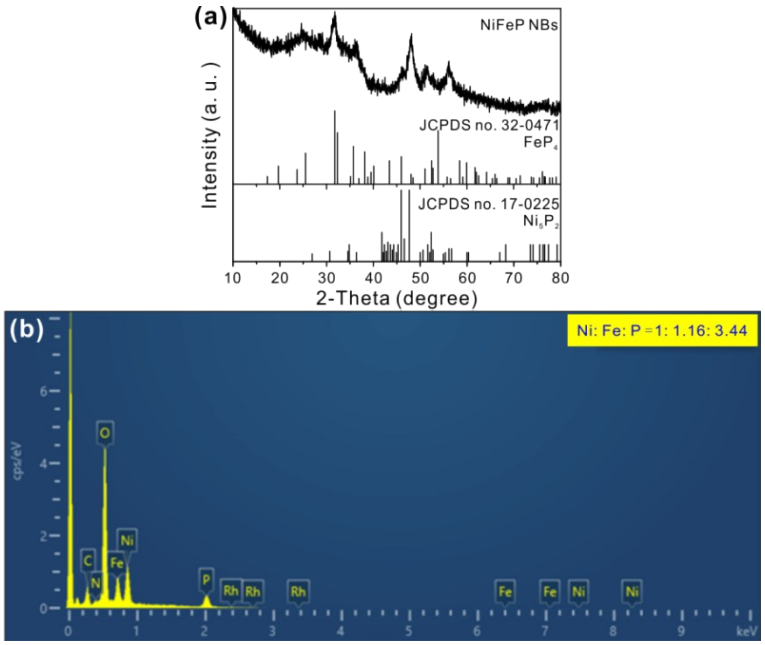

Fig. S6 (a) XRD pattern and (b) EDX spectrum of NiFeP NBs.

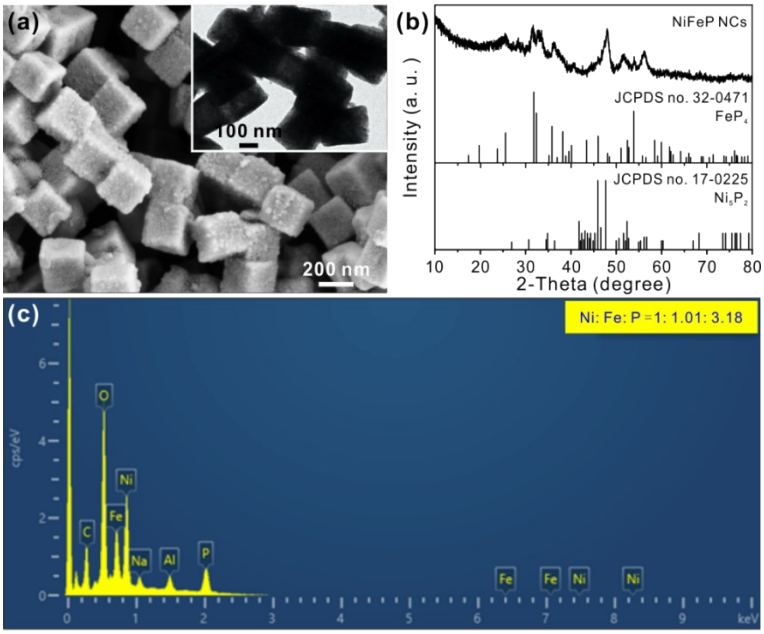

Fig. S7 (a) Large-scale SEM image, (b) XRD pattern, and (c) EDX spectrum of NiFeP NCs. The inset is the TEM image of NiFeP NCs.

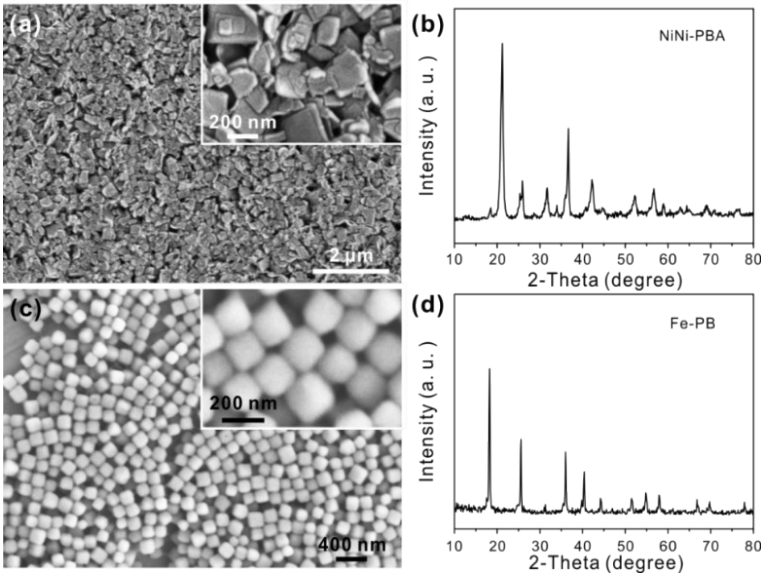

Fig. S8 (a,c) Large-scale SEM images of NiNi-PBA NPs (a) and Fe-PB NCs (c). (b,d) XRD patterns of NiNi-PBA NPs (b) and Fe-PB NCs (d). The inset of Fig. S8a and Fig. S8e is the high-magnification SEM image of NiNi-PBA NPs and Fe-PB NCs, respectively.

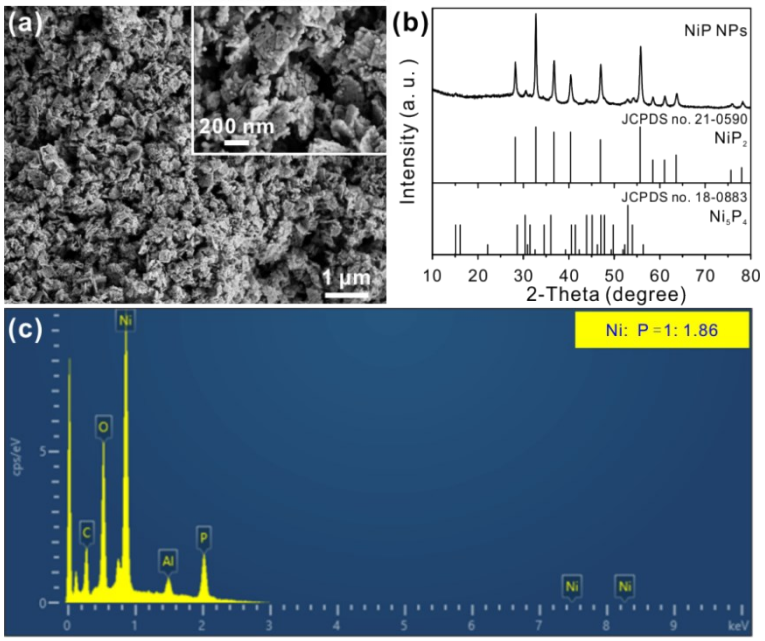

Fig. S9 (a) Large-scale SEM image, (b) XRD pattern, and (c) EDX spectrum of NiP NPs. The inset is the high-magnification SEM image of NiP NPs.

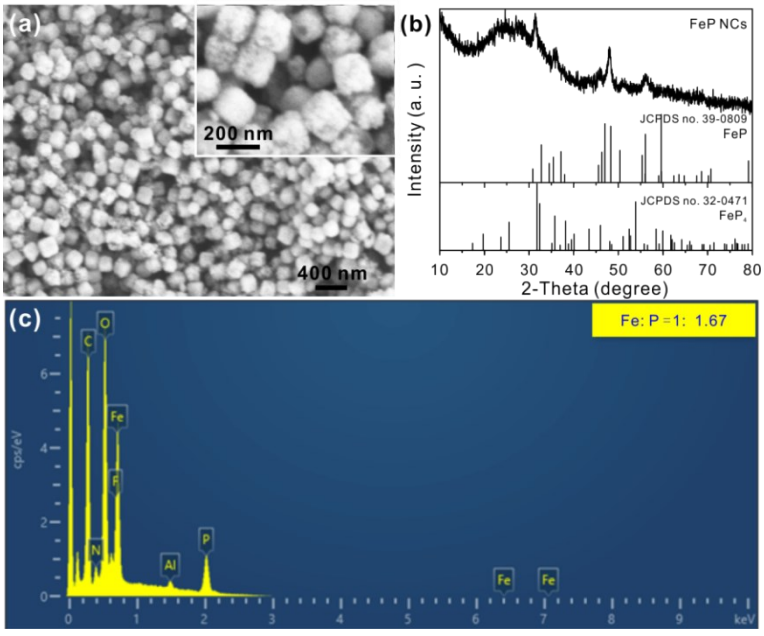

Fig. S10 (a) Large-scale SEM image, (b) XRD pattern, and (c) EDX spectrum of FeP NCs. The inset is the high-magnification SEM image of FeP NCs.

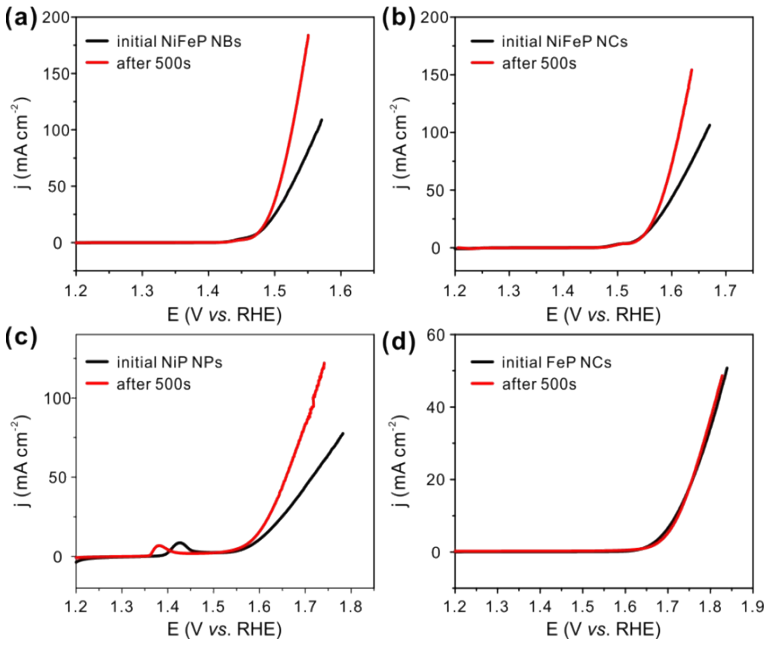

Fig. S11 LSV curves of NiFeP NBs (a), NiFeP NCs (b), NiP NPs (c), and FeP NCs before and after CA test on RDE at 10 mA cm^{-2}.

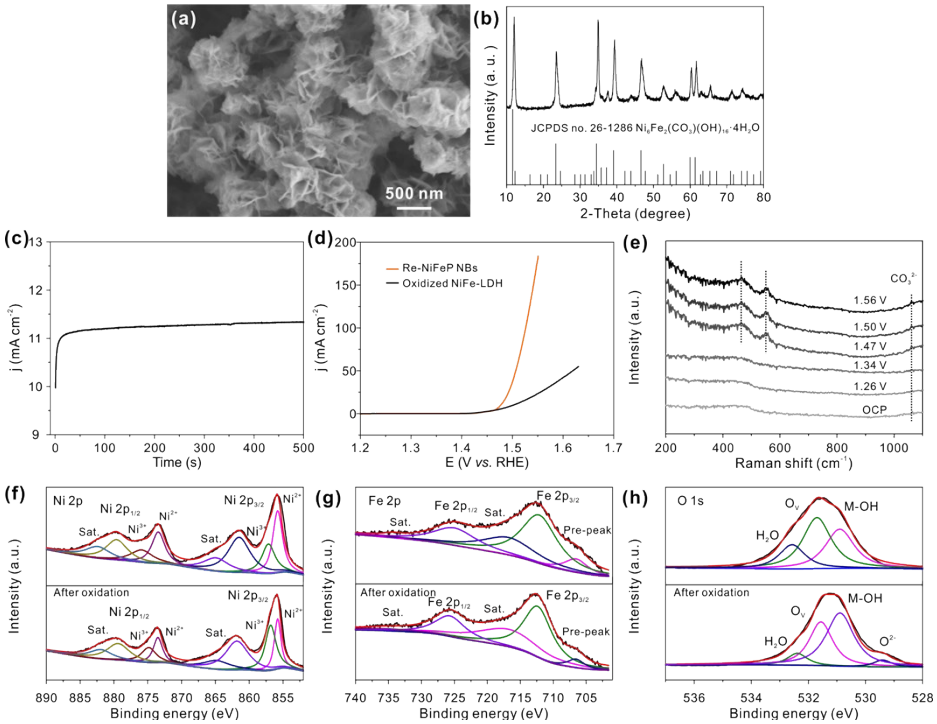

Fig. S12 (a) SEM image, (b) XRD pattern, and (c) CA test at 10 mA cm^{-2} of NiFe LDH. (d) LSV curves of reconstructed NiFeP NBs and electrochemically oxidized NiFe LDH. (e) *In-situ* Raman spectra of NiFe LDH at various potentials. (f-h) The high-resolution XPS spectra of NiFe LDH before and after electrochemical oxidation.

A one-step hydrothermal method is carried out to synthesize NiFe LDH (Fig. S12a and b). When loading the NiFe LDH on the RDE for CA test (Fig. S12c), obvious current density increase can be observed, indicating the occurrence of electrochemical oxidation. The Re-NiFeP NBs exhibits better OER performance than electrochemically oxidized NiFe LDH (Fig. S12d). The appearance of the two peaks at 462 and 553 cm^{-1} in the *in-situ* Raman spectra indicates the formation of NiOOH (Fig. S12e). The increase in Ni(III) and the emergence of O^{2-} after electrochemical oxidation also evidence the generation of metal oxyhydroxides (Fig. S12f-h).

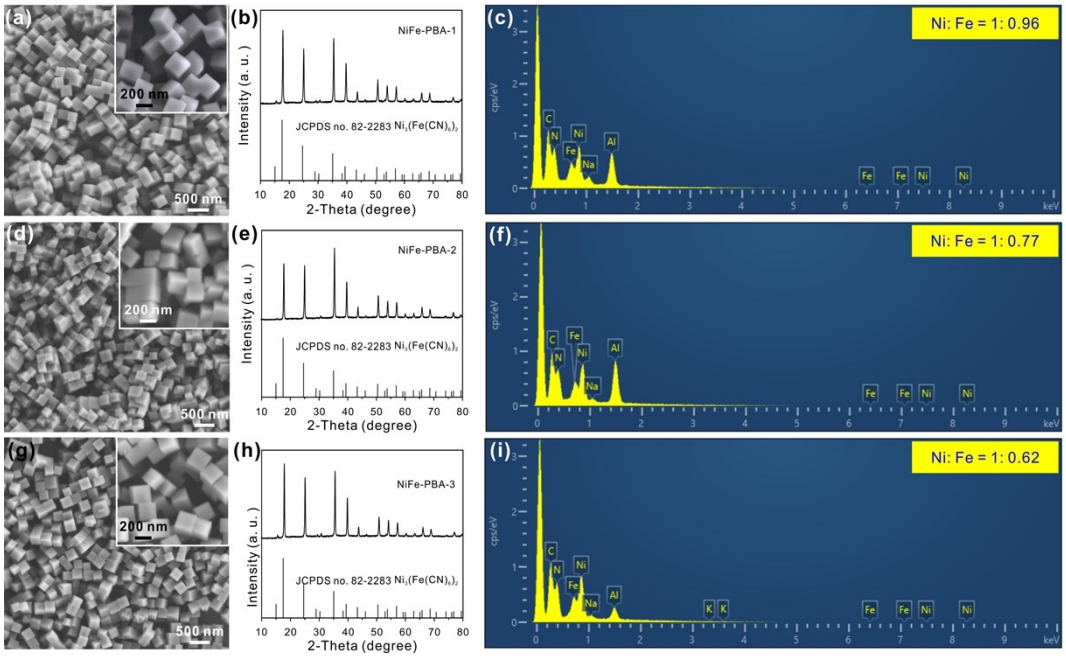

Fig. S13 (a,d,g) Large-scale SEM images, (b,e,h) XRD patterns, and (c,f,i) EDX spectra of NiFe-PBA-1 (a-c), NiFe-PBA-2 (d-f) and NiFe-PBA-3 (g-i).

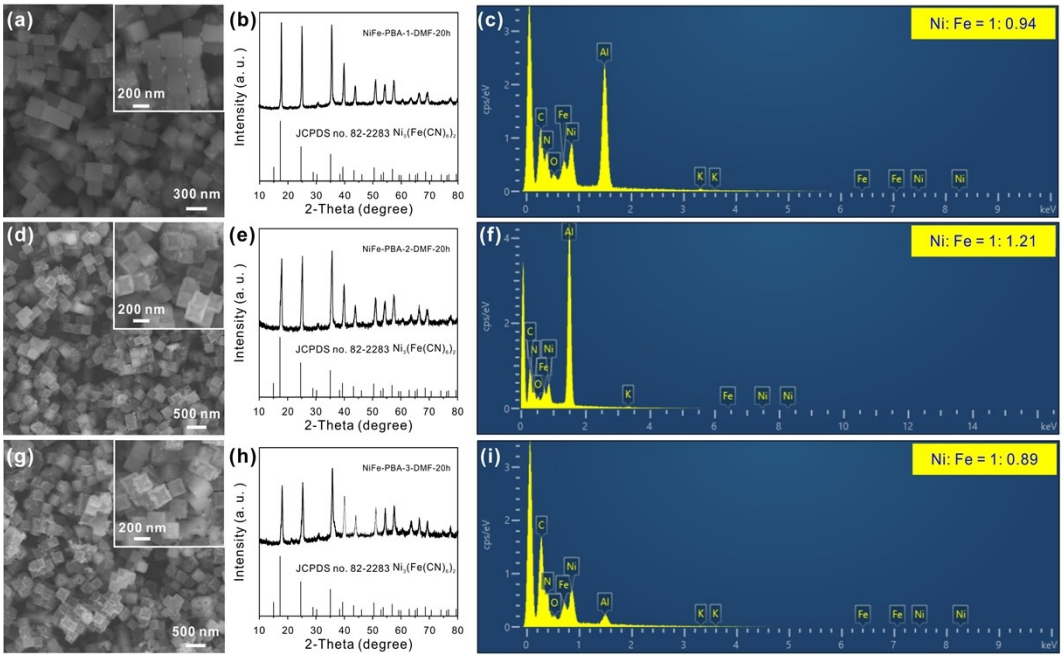

Fig. S14 (a,d,g) Large-scale SEM images, (b,e,h) XRD patterns, and (c,f,i) EDX spectra of NiFe-PBA-1-DMF-20 h (a-c), NiFe-PBA-2-DMF-20 h (d-f), and NiFe-PBA-3-DMF-20 h (g-i).

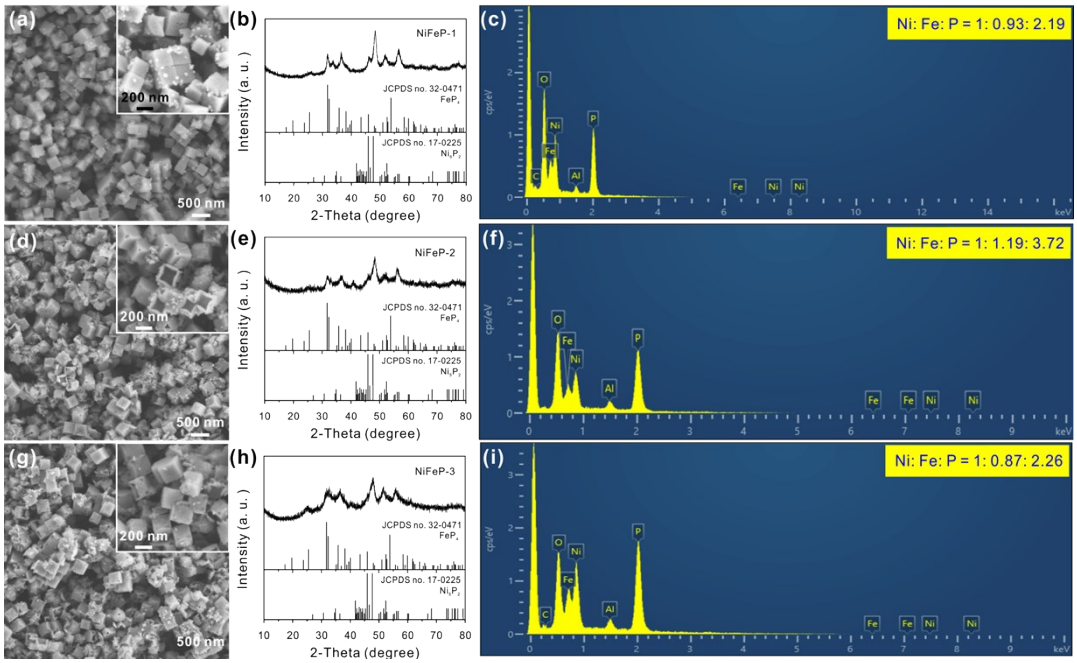

Fig. S15 (a,d,g) Large-scale SEM images, (b,e,h) XRD patterns, and (c,f,i) EDX spectra of NiFeP-1 (a-c), NiFeP-2 (d-f), and NiFeP-3 (g-i).

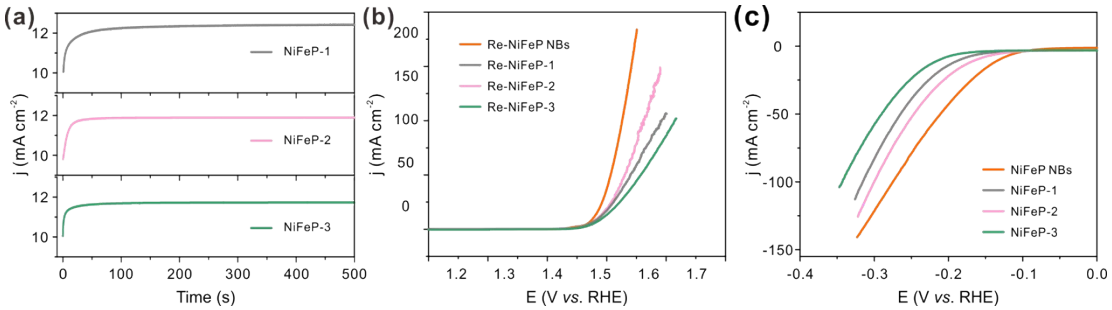

Fig. S16 (a) CA test at 10 mA cm^{-2} for NiFeP-1, NiFeP-2, and NiFeP-3. LSV curves of (b) OER and (c) HER for NiFeP-1, NiFeP-2, and NiFeP-3.

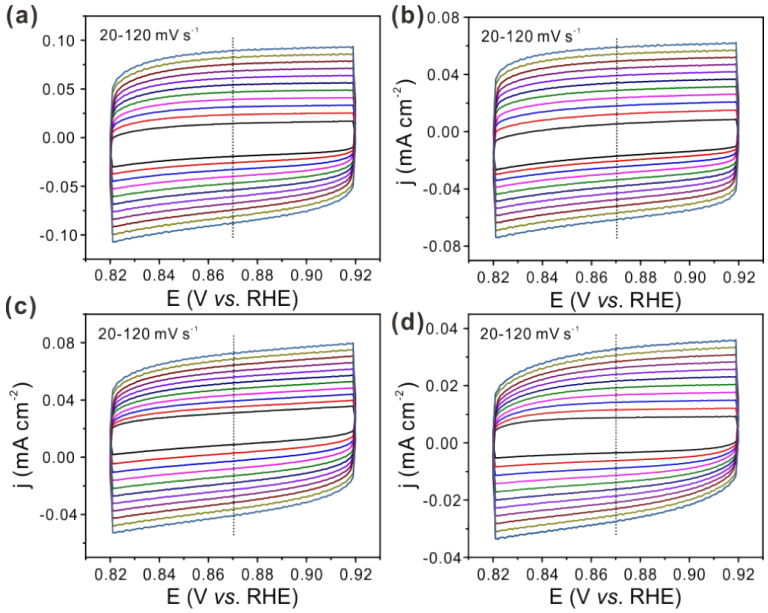

Fig. S17 CV curves of Re-NiFeP NBs (a), Re-NiFeP NCs (b), Re-NiP NPs (c), and Re-FeP NCs (d) at different scan rates from 20 to 120 mV s^{-1}.

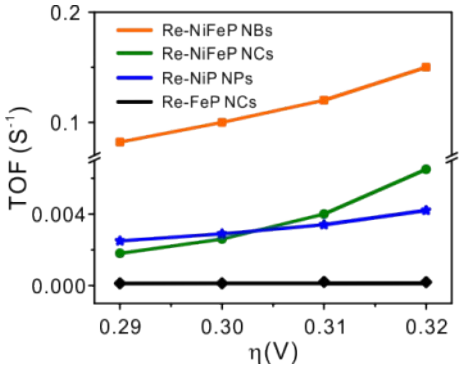

Fig. S18 TOFs of Re-NiFeP NBs, Re-NiFeP NCs, Re-NiP NPs, and Re-FeP NCs at η = 290, 300, 310 and 320 mV.

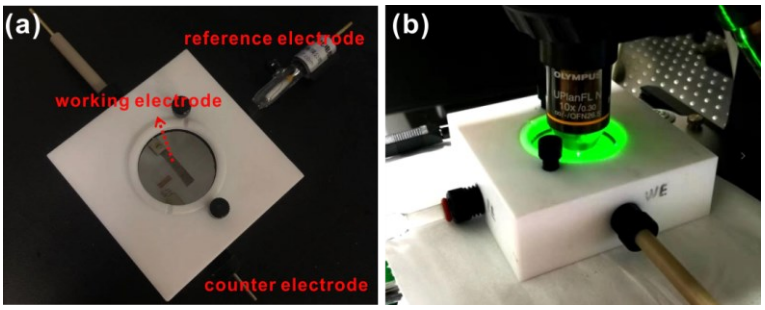

Fig. S19 (a) Physical diagram of *in-situ* Raman electrolysis cell and (b) the testing process of *In-situ* Raman spectroscopy.

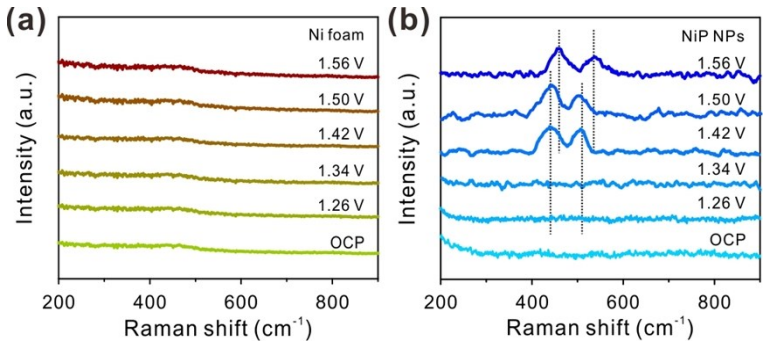

Fig. S20 *In-situ* Raman spectra of (a) Ni foam and (b) NiP NPs at various potentials during OER.

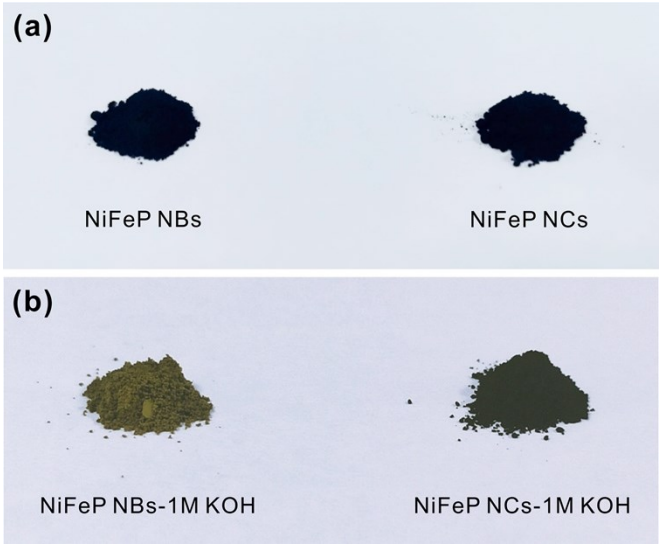

Fig. S21 Photographs of (a) NiFeP NBs and (b) NiFeP NCs before and after soaking in 1 M KOH for one day.

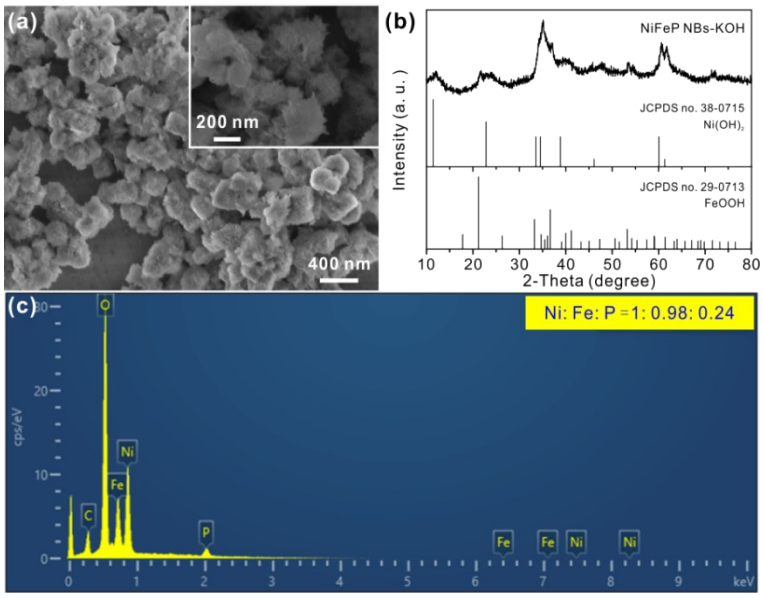

Fig. S22 (a) Large-scale SEM image, (b) XRD pattern, and (c) EDX spectrum of NiFeP NBs after soaking in 1 M KOH for one day. The inset is the high-magnification SEM image.

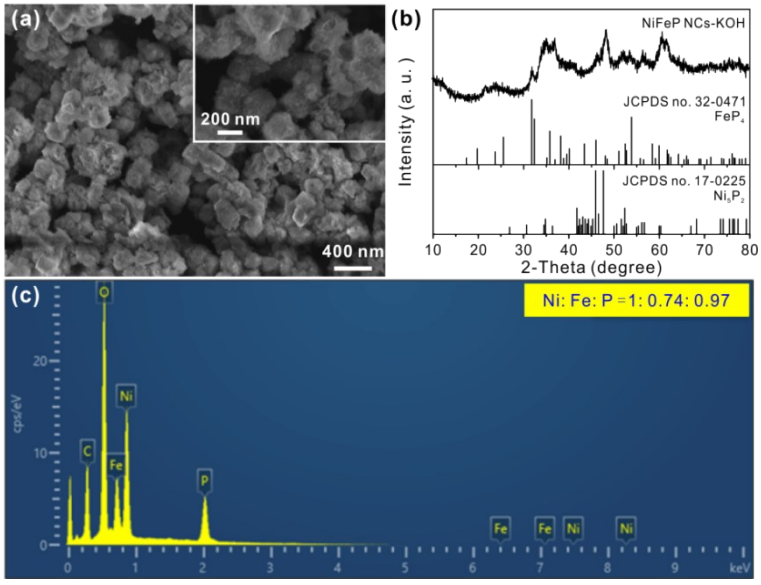

Fig. S23 (a) Large-scale SEM image, (b) XRD pattern, and (c) EDX spectrum of NiFeP NCs after soaking in 1 M KOH for one day. The inset is the high-magnification SEM image.

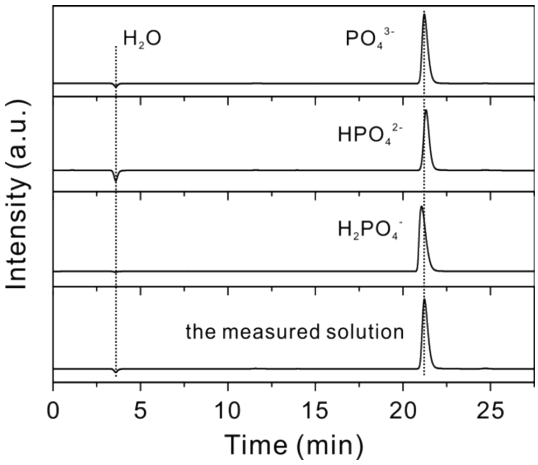

Fig. S24 Ion chromatographic curves of phosphorous-based anions for the solution collected after soaking the NiFeP NBs in alkaline solution for one day.

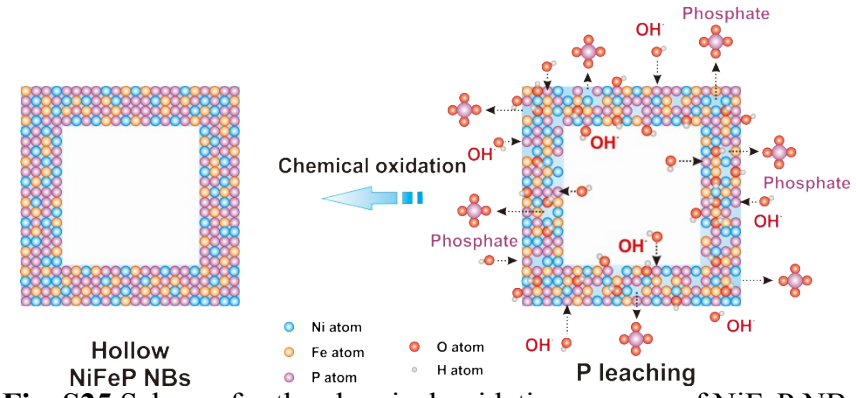

Fig. S25 Scheme for the chemical oxidation process of NiFeP NBs.

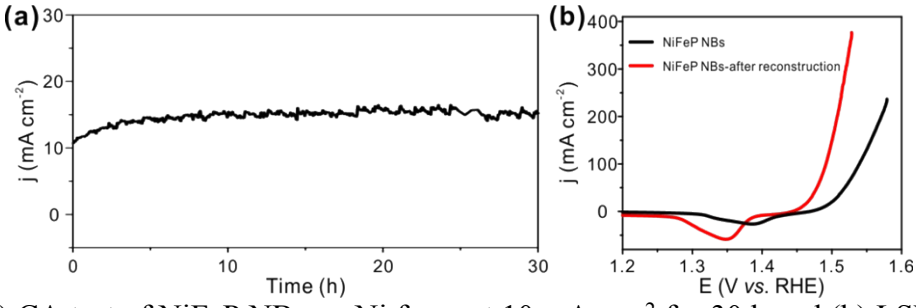

Fig. S26 (a) CA test of NiFeP NBs on Ni foam at 10 mA cm^{-2} for 30 h and (b) LSV curves of NiFeP NBs before and after reconstruction.

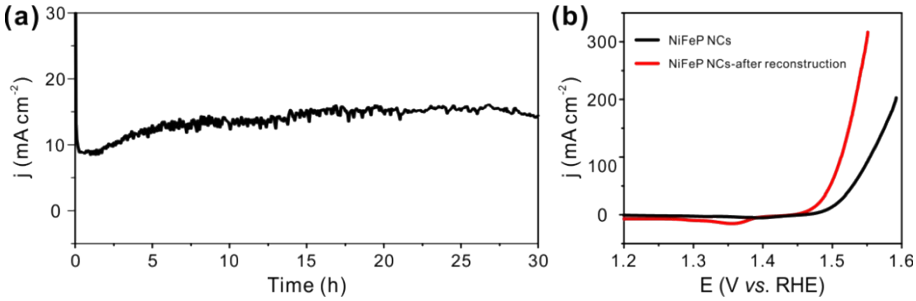

Fig. S27 (a) CA test of NiFeP NCs on Ni foam at 10 mA cm^{-2} for 30 h and (b) LSV curves of NiFeP NCs before and after reconstruction.

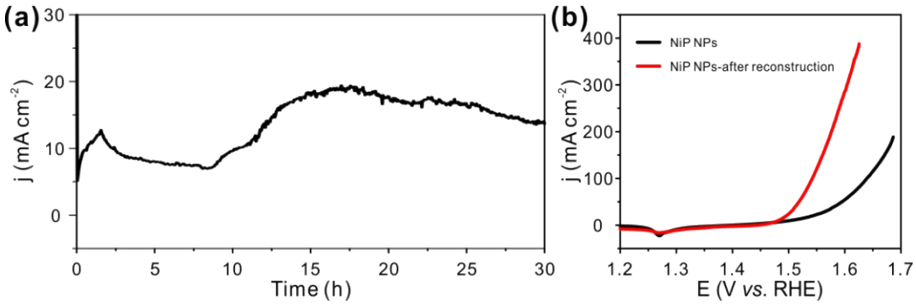

Fig. S28 (a) CA test of NiP NPs on Ni foam at 10 mA cm^{-2} for 30 h and (b) LSV curves of NiP NPs before and after reconstruction.

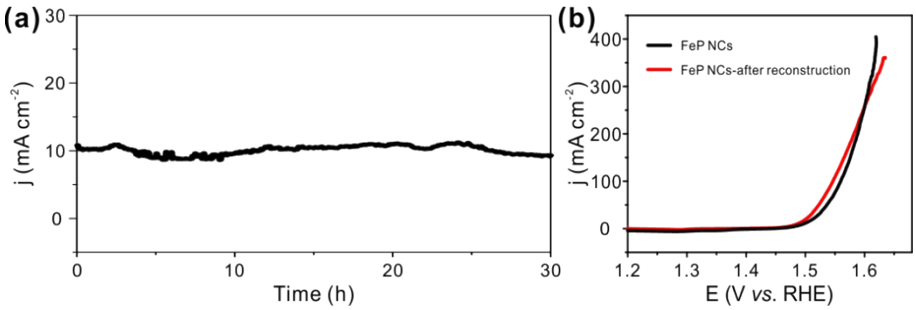

Fig. S29 (a) CA test of FeP NCs on Ni foam at 10 mA cm^{-2} for 30 h and (b) LSV curves of FeP NCs before and after reconstruction.

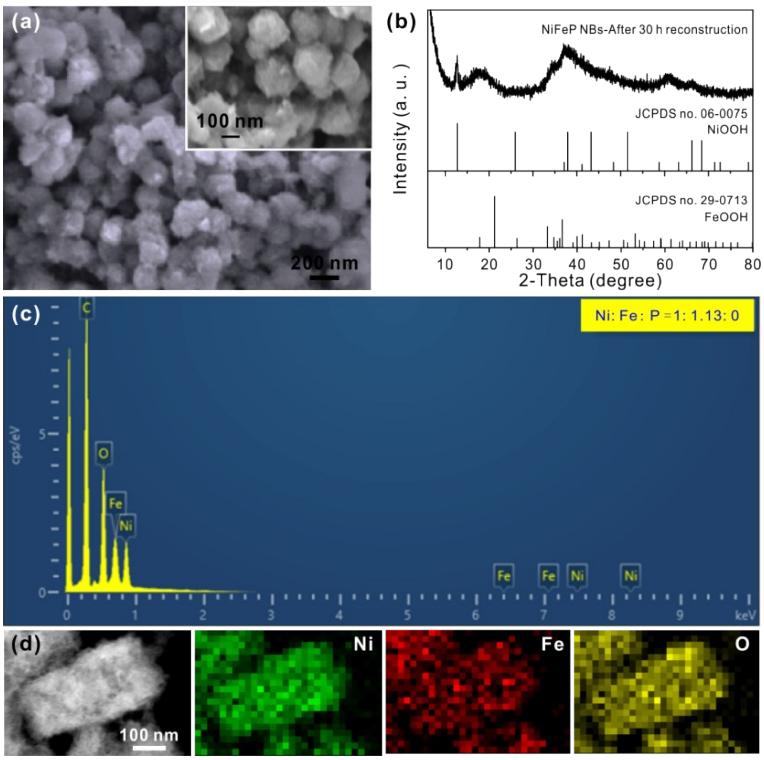

Fig. S30 (a) Large-scale SEM image, (b) XRD pattern, (c) EDX spectrum, and (d) HAADF-STEM image and corresponding elemental mapping images of Re-NiFeP NBs. The inset is the high-magnification SEM image.

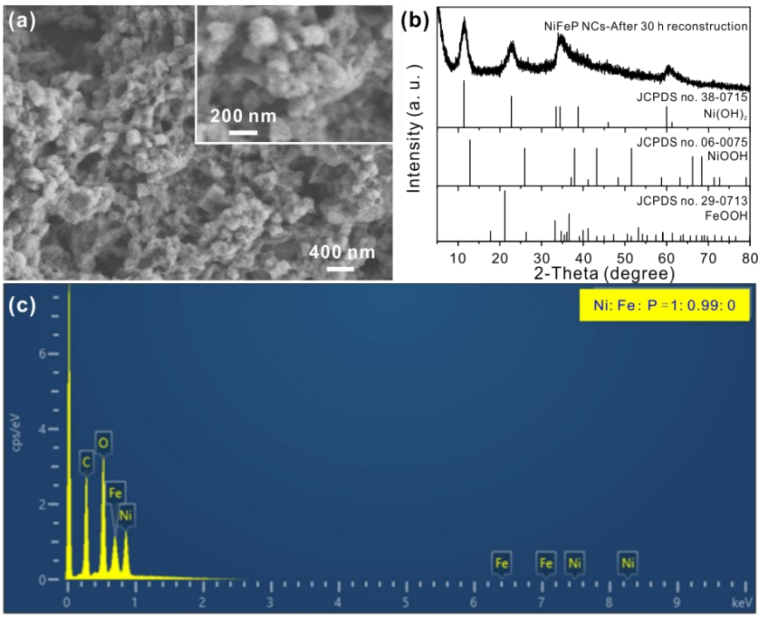

Fig. S31 (a) Large-scale SEM image, (b) XRD pattern, and (c) EDX spectrum of Re-NiFeP NCs. The inset is the high-magnification SEM image.

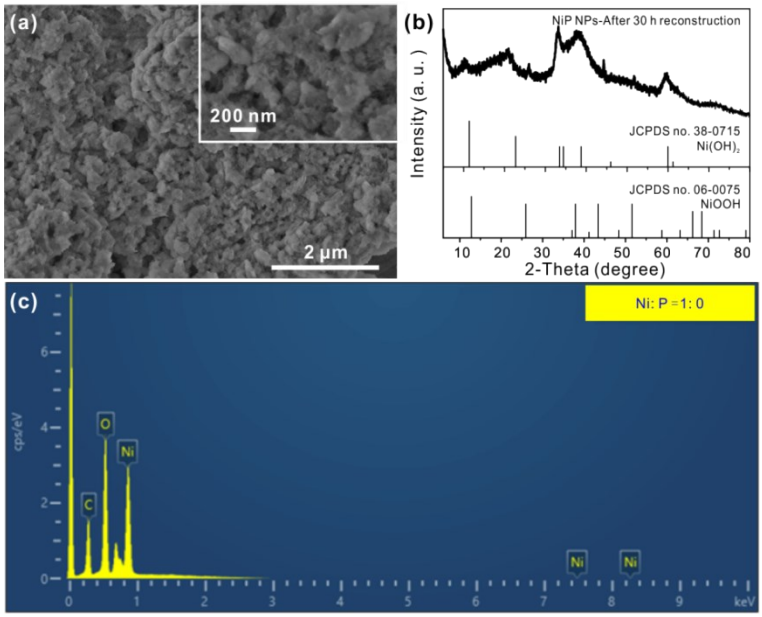

Fig. S32 (a) Large-scale SEM image, (b) XRD pattern, and (c) EDX spectrum of Re-NiP NPs. The inset is the high-magnification SEM image.

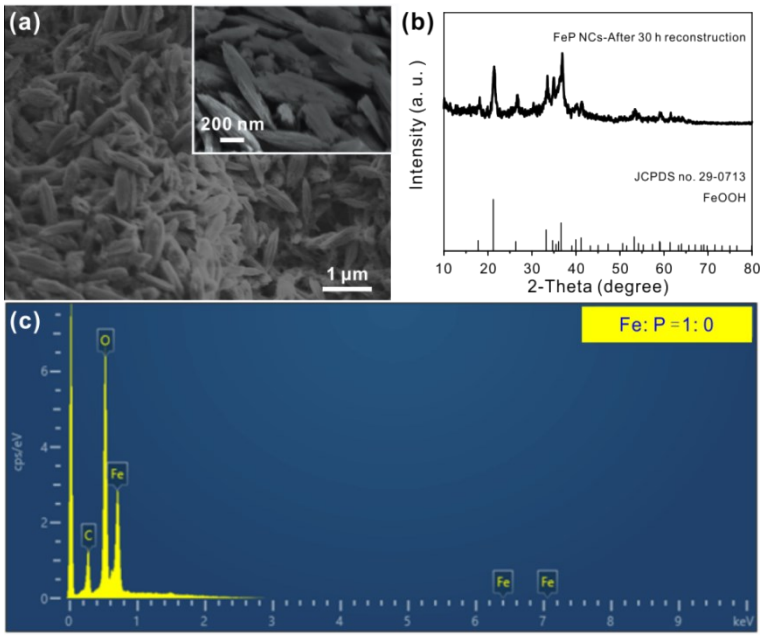

Fig. S33 (a) Large-scale SEM image, (b) XRD pattern, and (c) EDX spectrum of reconstructed FeP NCs. The inset of is the high-magnification SEM image.

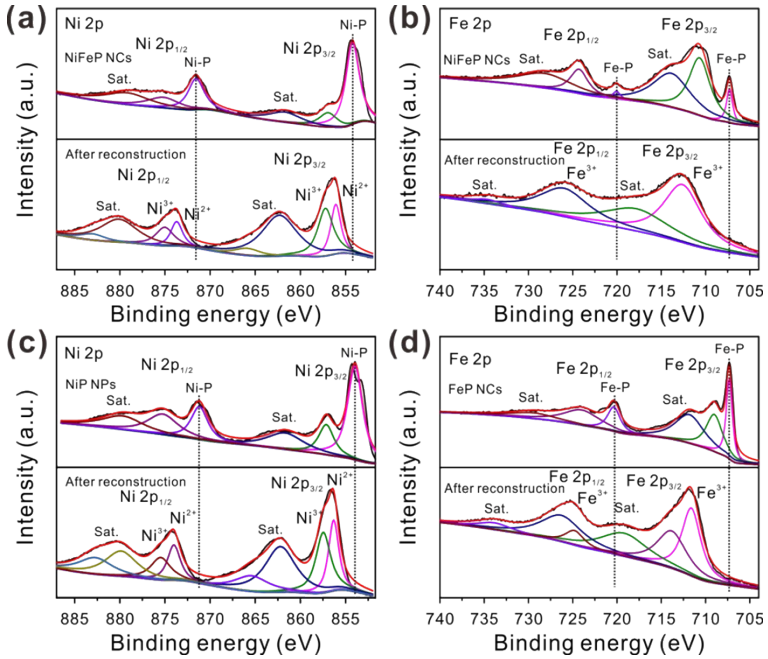

Fig. S34 The high-resolution XPS spectra of NiFeP NCs, NiP NPs, and FeP NCs before and after reconstruction: (a,b) Ni 2p and Fe 2p XPS spectra of NiFeP and Re-NiFeP NCs; (c) Ni 2p XPS spectra of NiP and Re-NiP NPs; (d) Fe 2p XPS spectra of FeP and Re-FeP NCs.

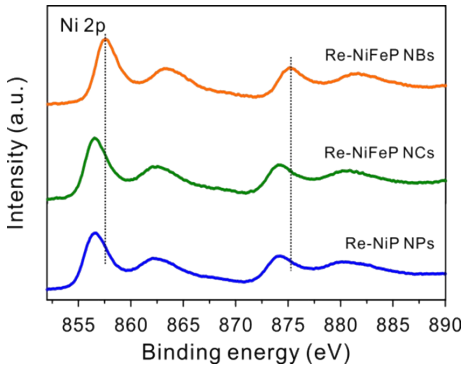

Fig. S35 Comparison of the Ni 2p XPS spectra of different catalysts after reconstruction.

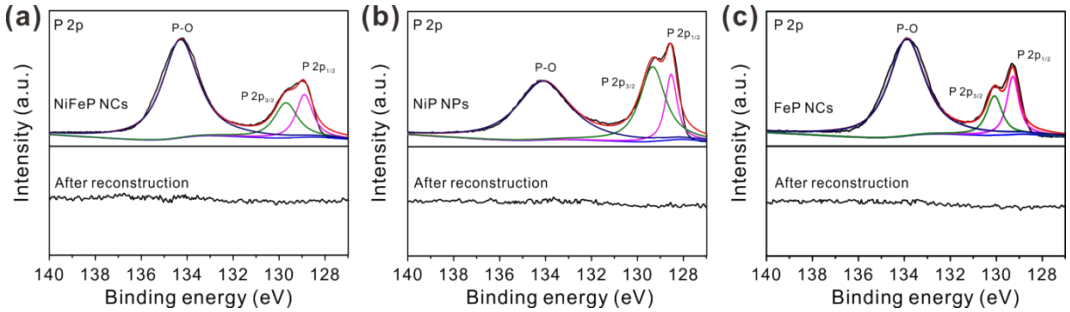

Fig. S36 The high-resolution P 2p XPS spectra of NiFeP NCs, NiP NPs, and FeP NCs before and after reconstruction: (a) NiFeP and Re-NiFeP NCs; (b) NiP and Re-NiP NPs; and (c) FeP and Re-FeP NCs.

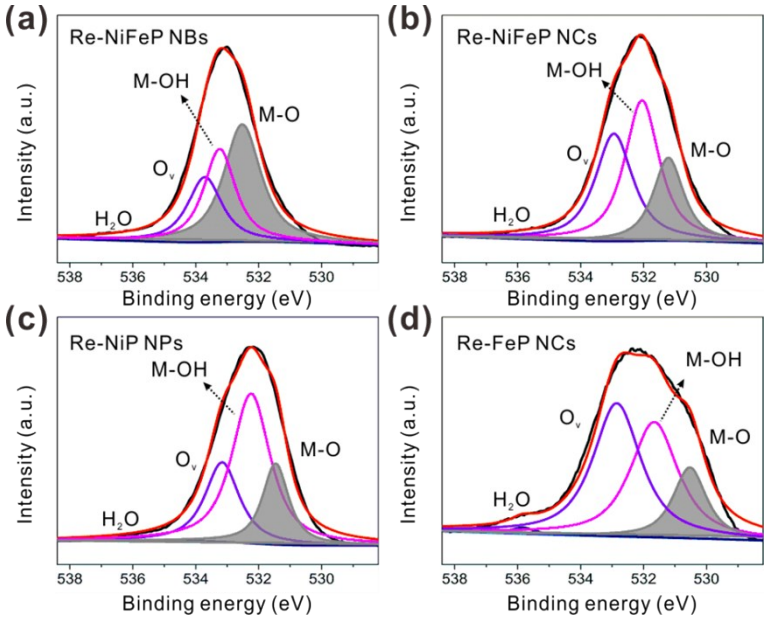

Fig. S37 The high-resolution O 1s XPS spectra of Re-NiFeP NBs (a), Re-NiFeP NCs (b), Re-NiP NPs (c), and Re-FeP NCs (d).

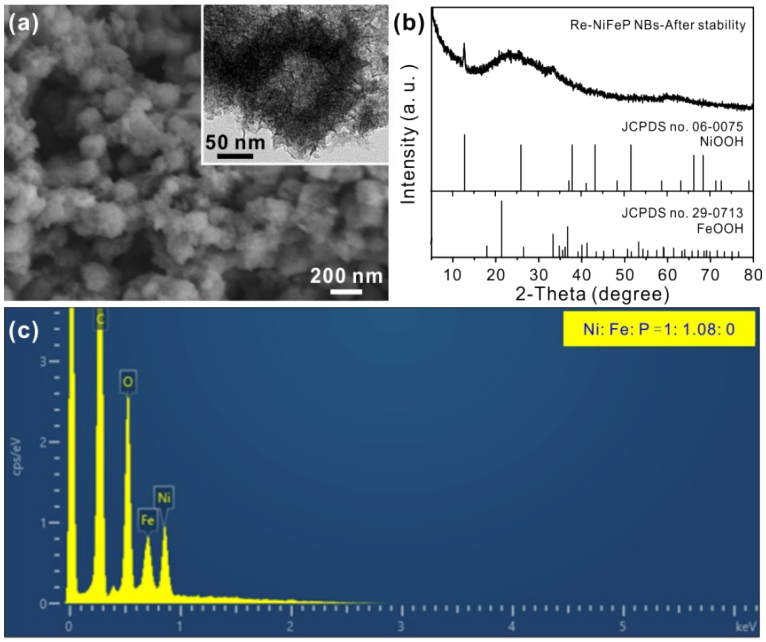

Fig. S38 (a) Large-scale SEM image, (b) XRD pattern, and (c) EDX spectrum of NiOOH/FeOOH NBs after OER stability test. The inset is the TEM image.

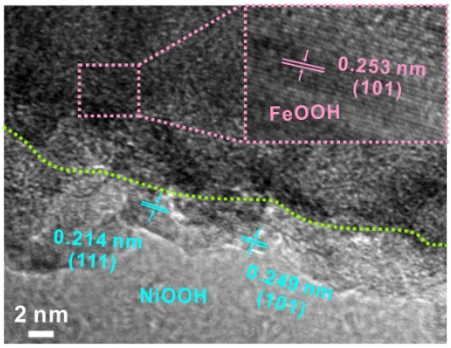

Fig. S39 The HRTEM image of NiOOH/FeOOH NBs after OER stability test.

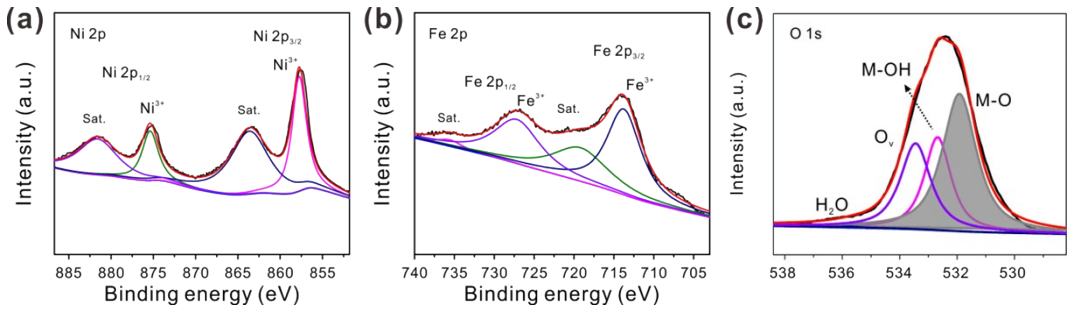

Fig. S40 The high-resolution XPS spectra of NiOOH/F eOOH NBs after OER stability test: (a) Ni 2p, (b) Fe 2p, and (c) O 1s.

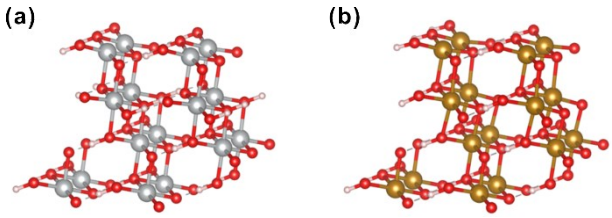

Fig. S41 Atomic model of NiOOH (a) and FeOOH (b). Brown balls: Fe atoms; Silvery balls: Ni atoms; Red balls: O atoms; White balls: H atoms.

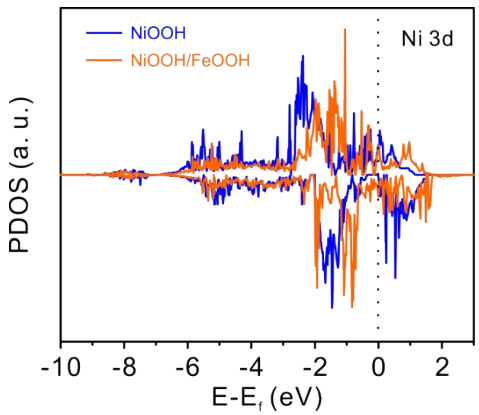

Fig. S42 The partial density of states (PDOS) of Ni 3d orbital for NiOOH and NiOOH/FeOOH, respectively.

$$H_2O + * \rightarrow OH^* + H^+ + e^- \quad (1)$$

$$OH^* \rightarrow O^* + H^+ + e^- \quad (2)$$

$$O^* + H_2O \rightarrow OOH^* + H^+ + e^- \quad (3)$$

$$OOH^* \rightarrow O_2 + H^+ + e^- \quad (4)$$

Fig. S43 Electron reaction paths for the single site of OER in NiOOH/FeOOH. Where * represents the active sites and OH*, O* and OOH* are the adsorbed intermediates.

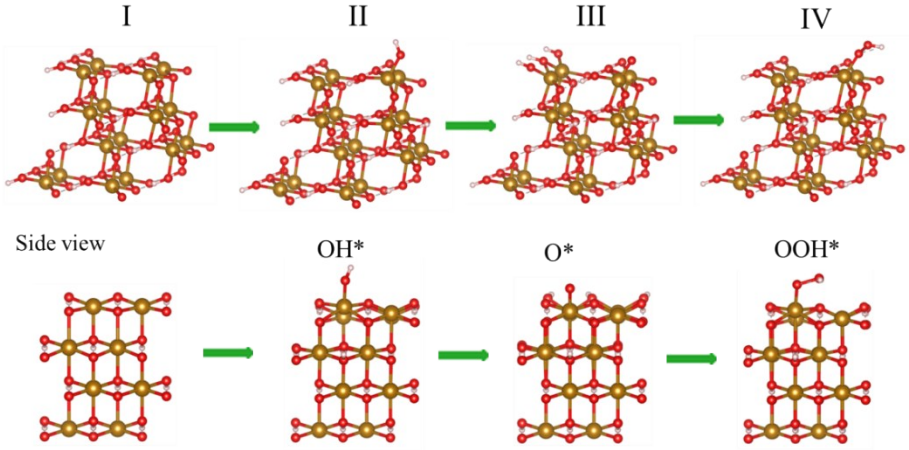

Fig. S44 Standard orientation (first row) and side views (second row) of the FeOOH model and the adsorbed OH*, O* and OOH* intermediates on the Fe site of FeOOH model. Brown balls: Fe atoms; Red balls: O atoms; White balls: H atoms.

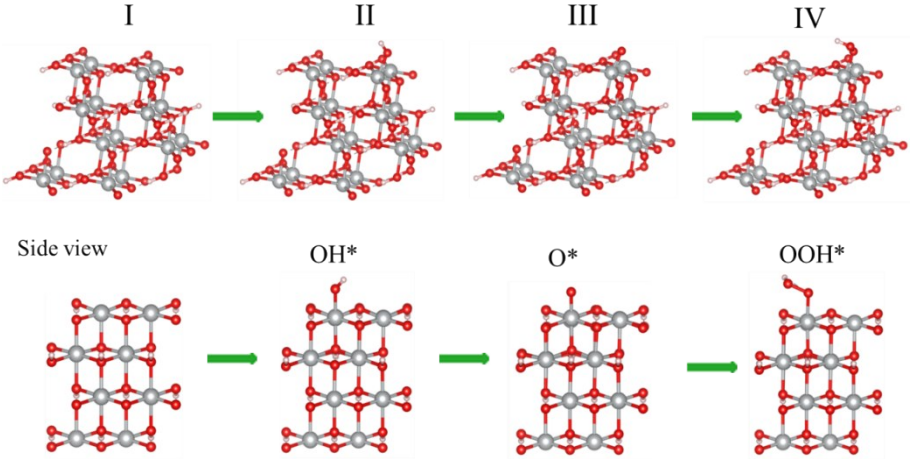

Fig. S45 Standard orientation (first row) and side views (second row) of the NiOOH model and the adsorbed OH*, O* and OOH* intermediates on the Ni site of NiOOH model. Silvery balls: Ni atoms; Red balls: O atoms; White balls: H atoms.

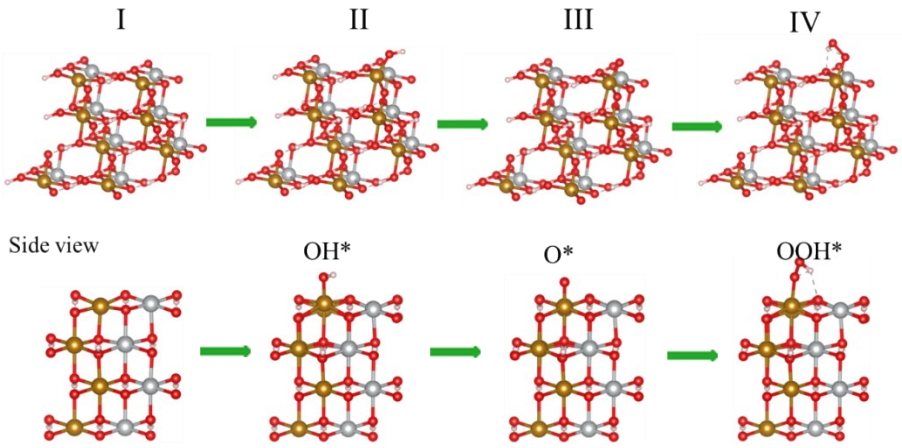

Fig. S46 Standard orientation (first row) and side views (second row) of the NiOOH/FeOOH model and the adsorbed OH*, O* and OOH* intermediates on the Fe site of NiOOH/FeOOH model. Brown balls: Fe atoms; Silvery balls: Ni atoms; Red balls: O atoms; White balls: H atoms.

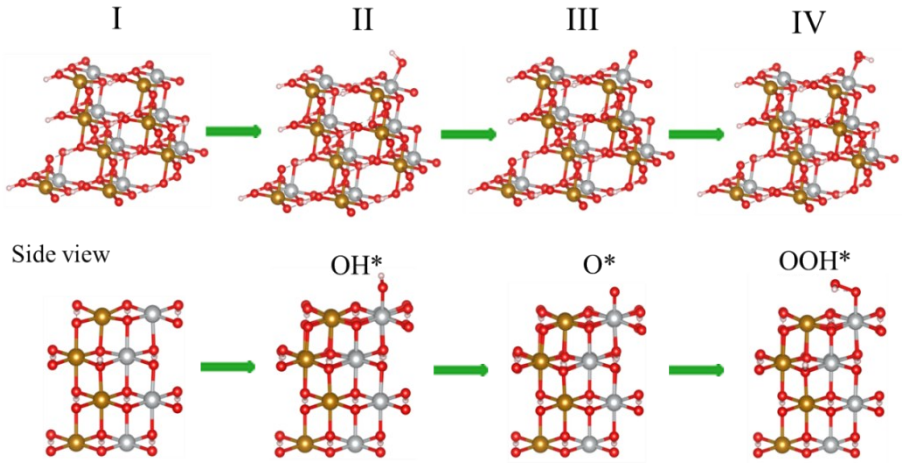

Fig. S47 Standard orientation (first row) and side views (second row) of the NiOOH/FeOOH model and the adsorbed OH*, O* and OOH* intermediates on the Ni site of NiOOH/FeOOH model. Brown balls: Fe atoms; Silvery balls: Ni atoms; Red balls: O atoms; White balls: H atoms.

(a)

$$Fe^{*} + Ni^{*} + H_2O \rightarrow Fe\text{-}OH^{*} + Ni^{*} + (H^{+} + e^{-}) \quad (1)$$

$$Fe\text{-}OH^{*} + Ni^{*} + H_2O \rightarrow Fe\text{-}OH^{*} + Ni\text{-}OH^{*} + (H^{+} + e^{-}) \quad (2)$$

$$Fe\text{-}OH^{*} + Ni\text{-}OH^{*} \rightarrow Fe\text{-}O^{*} + Ni\text{-}OH^{*} + (H^{+} + e^{-}) \quad (3)$$

$$Fe\text{-}O^{*} + Ni\text{-}OH^{*} \rightarrow Fe^{*} + Ni^{*} + O_2 + (H^{+} + e^{-}) \quad (4)$$

(b)

$$Fe^{*} + Ni^{*} + H_2O \rightarrow Fe\text{-}OH^{*} + Ni^{*} + (H^{+} + e^{-}) \quad (1)$$

$$Fe\text{-}OH^{*} + Ni^{*} + H_2O \rightarrow Fe\text{-}OH^{*} + Ni\text{-}OH^{*} + (H^{+} + e^{-}) \quad (2)$$

$$Fe\text{-}OH^{*} + Ni\text{-}OH^{*} \rightarrow Fe\text{-}OH^{*} + Ni\text{-}O^{*} + (H^{+} + e^{-}) \quad (3)$$

$$Fe\text{-}O^{*} + Ni\text{-}OH^{*} \rightarrow Fe^{*} + Ni^{*} + O_2 + (H^{+} + e^{-}) \quad (4)$$

(c)

$$Fe^{*} + Ni^{*} + H_2O \rightarrow Fe^{*} + Ni\text{-}OH^{*} + (H^{+} + e^{-}) \quad (1)$$

$$Fe\text{-}OH^{*} + Ni^{*} + H_2O \rightarrow Fe\text{-}OH^{*} + Ni\text{-}OH^{*} + (H^{+} + e^{-}) \quad (2)$$

$$Fe\text{-}OH^{*} + Ni\text{-}OH^{*} \rightarrow Fe\text{-}O^{*} + Ni\text{-}OH^{*} + (H^{+} + e^{-}) \quad (3)$$

$$Fe\text{-}O^{*} + Ni\text{-}OH^{*} \rightarrow Fe^{*} + Ni^{*} + O_2 + (H^{+} + e^{-}) \quad (4)$$

(d)

$$Fe^{*} + Ni^{*} + H_2O \rightarrow Fe^{*} + Ni\text{-}OH^{*} + (H^{+} + e^{-}) \quad (1)$$

$$Fe\text{-}OH^{*} + Ni^{*} + H_2O \rightarrow Fe\text{-}OH^{*} + Ni\text{-}OH^{*} + (H^{+} + e^{-}) \quad (2)$$

$$Fe\text{-}OH^{*} + Ni\text{-}OH^{*} \rightarrow Fe\text{-}OH^{*} + Ni\text{-}O^{*} + (H^{+} + e^{-}) \quad (3)$$

$$Fe\text{-}O^{*} + Ni\text{-}OH^{*} \rightarrow Fe^{*} + Ni^{*} + O_2 + (H^{+} + e^{-}) \quad (4)$$

Fig. S48 Possible response pathways for the dual sites of OER in NiOOH/FeOOH: (a) pathway 1, (b) pathway 2, (c) pathway 3 and (d) pathway 4. Where * represents the active sites and OH*, (OH* + OH*), and (O* + OH*) are adsorbed intermediates.

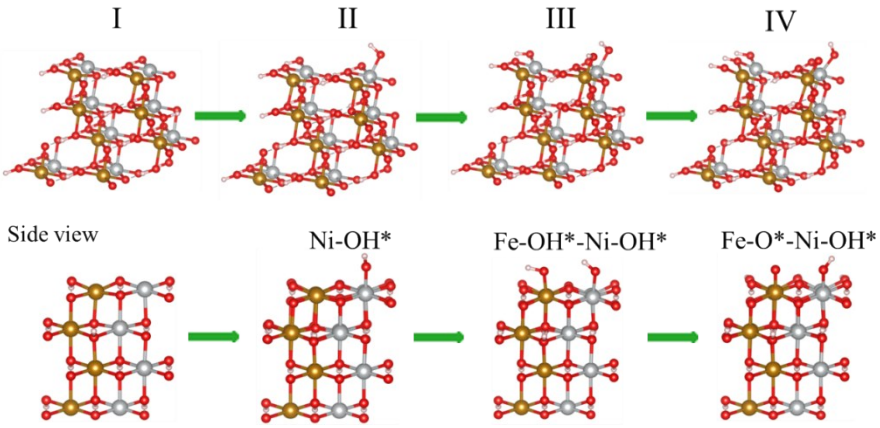

Fig. S49 Standard orientation (first row) and side views (second row) of the NiOOH/FeOOH model and the adsorbed OH*, O* and OOH* intermediates on the Fe-Ni dual sites 2 of NiOOH/FeOOH model. Brown balls: Fe atoms; Silvery balls: Ni atoms; Red balls: O atoms; White balls: H atoms.

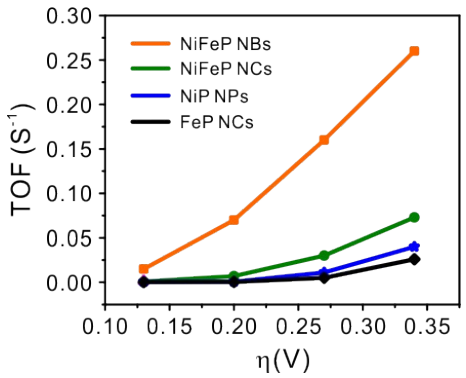

Fig. S50 TOFs for HER of NiFeP NBs, NiFeP NCs, NiP NPs, and FeP NCs at η = 290, 300, 310, and 320 mV.

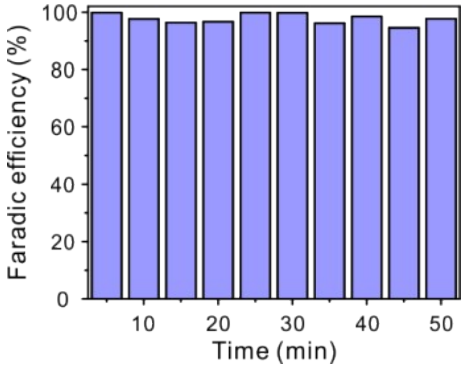

Fig. S51 FE of H_2 for NiFeP NBs as a function of time at the current density of 10 mA cm^{-2}.

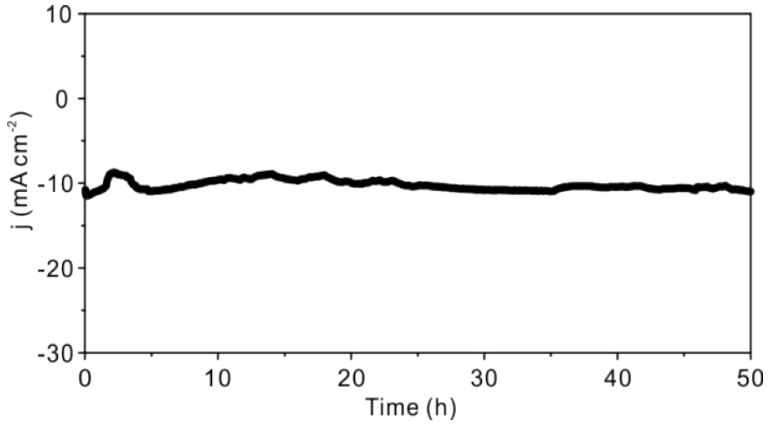

Fig. S52 The HER stability test of NiFeP NBs .

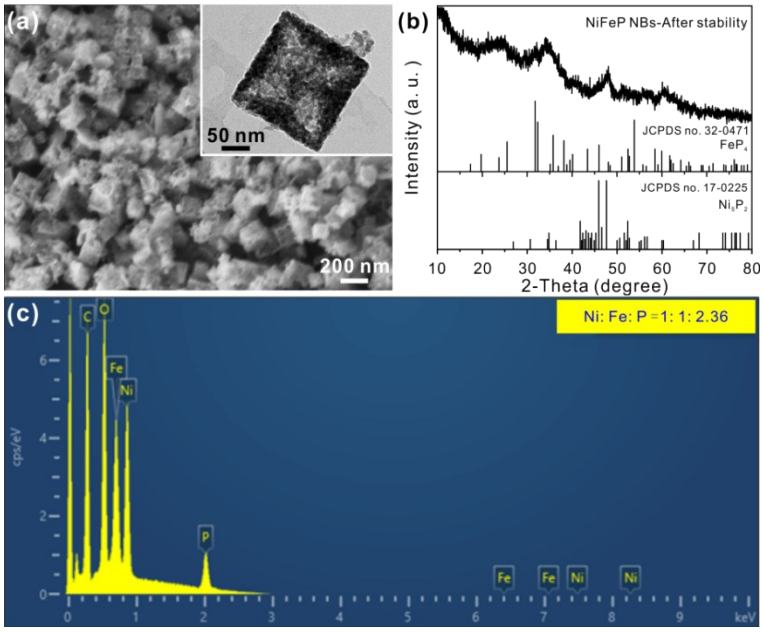

Fig. S53 (a) Large-scale SEM image, (b) XRD pattern, and (c) EDX spectrum of NiFeP NBs after HER stability test. The inset is the TEM image of NiFeP NBs.

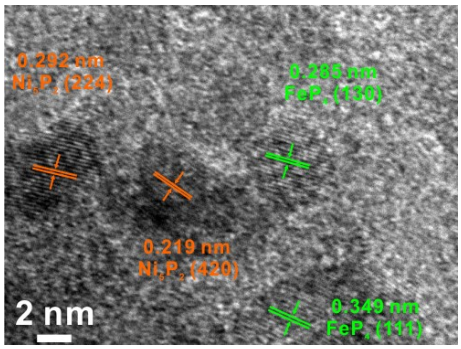

Fig. S54 HRTEM image of NiFeP NBs after HER stability test.

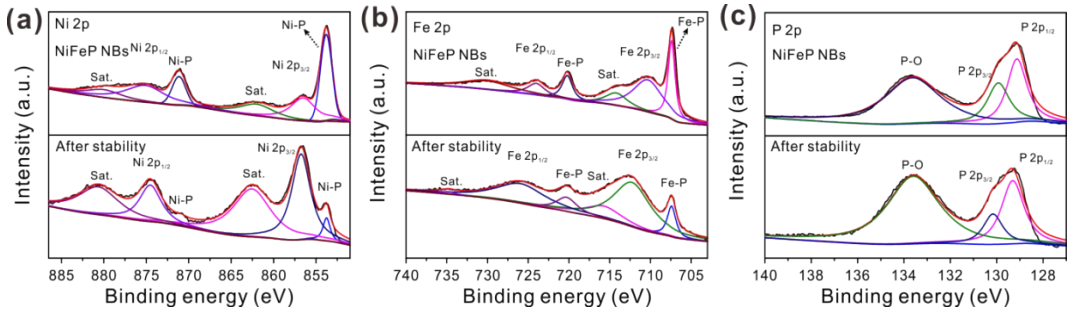

Fig. S55 The high-resolution XPS spectra of NiFeP NBs before and after HER durability test: (a) Ni 2p, (b) Fe 2p, and (c) P 2p.

Table S1 The OER overpotentials of the reconstructed metal phosphides on RDE and Ni foam.

Catalysts	Overpotentialson RDE(mV)		Overpotentialson Ni foam(mV)	
	10 mA cm^{-2}	100 mA cm^{-2}	10 mA cm^{-2}	100 mA cm^{-2}
NiOOH/FeOOH NBs	246	296	228	261
Re-NiFeP NCs	316	383	240	282
Re-NiP NPs	352	488	252	312
Re-FeP NCs	494	/	267	329

Table S2 Comparisons for the OER overpotential of NiOOH/FeOOH NBs on RDE and Ni foam with that of other reported catalysts.

Catalysts	Overpotentials on RDE(mV)		Overpotentials on Ni foam (mV)		Ref.
	10 mA cm^{-2}	100 mA cm^{-2}	10 mA cm^{-2}	100 mA cm^{-2}	
NiOOH/FeOOH NBs	**246**	**296**	**228**	**261**	**This work**
Fe-Co-P	269	/	/	/	10
$Co_{0.6}Fe_{0.4}P$-1.125	298	/	/	/	11
DR-NiOOH	/	/	281	/	12
NiFeOOH/NiFe-LDH	/	/	/	290	13
C-(Fe-Ni)P@PC/(Ni-Co)P@CC	251	/	/	/	14
CR-NiOOH	/	/	278	/	15
CoFeP NFs/NPCNT	278	/	/	/	16
Zn;$NiFeO_xH_y$	/	/	250	/	17
FeP_4 cubes	283	/	/	/	18
V_{CN}-mediated PBA	283	/	/	/	19
$Ni_{0.8}Co_{0.1}Fe_{0.1}O_xH_y$	/	/	239	/	20
$FeNi(VO_4)x$@NF	/	/	/	274	21
P/Mo-Co_3O_4@CC	/	/	265	/	22
$Ni11(HPO_3)_8(OH)_6$/NF	/	/	232	362	23
$Na_2Co_{0.75}Fe_{0.25}P_2O_7$/C NPs	300	/	/	/	24
Ni10-CoPi	320	/	/	/	25
CoS_x/FeS_x	304	/	/	/	26
$CoSe_2$–D_{Fe}–V_{Co}	294	/	/	/	27

Table S3 The free energy change (ΔG) of each elementary reaction for OER on different catalysts at U = 0 V.

Models	Sites	ΔG_1 (eV)	ΔG_2 (eV)	ΔG_3 (eV)	ΔG_4 (eV)
FeOOH	Fe site	-0.08	0.64	2.46	1.9
NiOOH	Ni site	1.35	2.17	0.69	0.71
NiOOH/FeOOH	Fe site	0.94	1.19	2.15	0.64
	Ni site	1.17	1.29	1.57	0.89
	Fe-Ni dual sites 1	0.94	1.28	1.36	1.34
	Fe-Ni dual sites 2	1.17	1.05	1.36	1.34

Table S4 The free energy change (ΔG) of each elementary reaction for OER on different catalysts at U = 1.23 V.

Models	Sites	ΔG_1 (eV)	ΔG_2 (eV)	ΔG_3 (eV)	ΔG_4 (eV)
FeOOH	Fe site	-1.31	-0.59	1.23	0.67
NiOOH	Ni site	0.12	0.94	-0.54	-0.52
NiOOH/FeOOH	Fe site	-0.29	-0.04	0.92	-0.59
	Ni site	-0.06	0.06	0.34	-0.34
	Fe-Ni dual sites 1	-0.29	0.05	0.13	0.11
	Fe-Ni dual sites 2	-0.06	-0.18	0.13	0.11

Table S5 The comparasion for the HER overpotentials of electro-catalysts on RDE and Ni foam.

Catalysts	Overpotentials on RDE(mV)		Overpotentials on Ni foam(mV)	
	10 mA cm^{-2}	100 mA cm^{-2}	10 mA cm^{-2}	100 mA cm^{-2}
NiFeP NBs	131	275	110	215
NiFeP NCs	213	374	111	259
NiP NPs	286	/	125	310
FeP NCs	273	/	213	331

Table S6 Comparisons of overall water splitting performance with other reported electrocatalysts.

Catalysts	Cell Voltages (V, 10 mA cm^{-2})	Ref.
NiOOH/FeOOH NBs||NiFeP NBs	**1.53**	**This work**
NiFeSP/NF	1.58	[28]
FNP	1.63	[29]
$Co_{0.6}Fe_{0.4}P$	1.57	[11]
Ni-Co-P	1.62	[30]
Co_4Ni_1P	1.59	[31]
CoP-InNC@CNT	1.58	[32]
$Ni_{0.8}Co_{0.1}Fe_{0.1}O_xH_y\|\|Ni_{0.9}Co_{0.1}O_xH_y$	1.58	[20]
SNCF-NRs	1.68	[33]
$NiCo_2O_4$	1.65	[34]
NiCoP	1.58	[35]
$Ni_{0.33}Co_{0.67}MoS_4$/CFC	1.55	[36]
MoS_2-NiS_2/NGF	1.64	[37]
CVN/CC	1.64	[38]
NiFeOH/CoS_x/NF	1.56	[39]
MoS_2/NiS_2 nanosheets	1.59	[40]
$Co_{0.9}S_{0.58}P_{0.42}$	1.59	[41]
NiCoFeB	1.81	[42]
$NiCo_2O_4$@$CoMoO_4$/NF	1.55	[43]
V-CoP@a-CeO_2	1.56	[44]

Reference

1. Y. Lian, H. Sun, X. Wang, P. Qi, Q. Mu, Y. Chen, J. Ye, X. Zhao, Z. Deng, Y. Peng, Chem. Sci., 2019, 10, 464-474.

2. J. Nai, Y. Lu, X. Y. Yu, J. Mater. Chem. A, 2018, 6, 21891-21895.

3. Y. Tang, Q. Liu, L. Dong, H.B. Wu, X. Y. Yu, Appl. Catal. B: Environ., 2020, 266, 118627.

4. G. Kresse, J. Furthmüller, Comput. Mater. Sci., 1996, 6, 15-50.

5. P. E. Blöchl, Phys. Rev. B, 1994, 50, 17953-17979.

6. J. P. Perdew, K. Burke, M. Ernzerhof, Phys. Rev. Lett., 1996, 77, 3865-3868.

7. S. Grimme, J. Antony, S. Ehrlich, H. Krieg, J. Chem. Phys., 2010, 132, 154104.

8. H. J. Monkhorst, J. D. Pack, Phys. Rev. B, 1976, 13, 5188-5192.

9. J.K. Nørskov, J. Rossmeisl, A. Logadottir, L. Lindqvist, J.R. Kitchin, T. Bligaard, H.J.K. Jonsson, J. Phys. Chem. B, 2004, 108, 17886-17892.

10. H. Zhang, W. Zhou, J. Dong, X.F. Lu, X.W. Lou, Energy Environ. Sci., 2019, 12, 3348-3355.

11. Y. Lian, H. Sun, X. Wang, P. Qi, Q. Mu, Y. Chen, J. Ye, X. Zhao, Z. Deng, Y. Peng, Chem. Sci., 2019, 10, 464-474.

12. X. Liu, K. Ni, B. Wen, R. Guo, C. Niu, J. Meng, Q. Li, P. Wu, Y. Zhu, X. Wu, L. Mai, ACS Energy Lett., 2019, 4, 2585-2592.

13. Y. Wang, Y. Zhu, S. Zhao, S. She, F. Zhang, Y. Chen, T. Williams, T. Gengenbach, L. Zu, H. Mao, W. Zhou, Z. Shao, H. Wang, J. Tang, D. Zhao, C. Selomulya, Matt., 2020, 3, 2124-2137.

14. C.N. Lv, L. Zhang, X.H. Huang, Y.X. Zhu, X. Zhang, J.S. Hu, S.Y. Lu, Nano Energy, 2019, 65, 103995.

15. X. Liu, J. Meng, K. Ni, R. Guo, F. Xia, J. Xie, X. Li, B. Wen, P. Wu, M. Li, J. Wu, X. Wu, L. Mai, D. Zhao, Cell Reports Phys. Sci., 2020, 1, 100241.

16. W. Li, Y. Chen, B. Yu, Y. Hu, X. Wang, D. Yang, Nanoscale, 2019, 11, 17031-17040.

17. S.Y. Lim, S. Park, S.W. Im, H. Ha, H. Seo, K.T. Nam, ACS Catal., 2020, 10, 235-244.

18. Q. He, H. Xie, Z.u. Rehman, C. Wang, P. Wan, H. Jiang, W. Chu, L. Song, ACS Energy Lett., 2018, 3, 861-868.

19. Z.Y. Yu, Y. Duan, J.D. Liu, Y. Chen, X.K. Liu, W. Liu, T. Ma, Y. Li, X.S. Zheng, T. Yao, M.R. Gao, J.F. Zhu, B.J. Ye, S.H. Yu, Nat. Commun., 2019, 10, 2799.

20. Q. Zhao, J. Yang, M. Liu, R. Wang, G. Zhang, H. Wang, H. Tang, C. Liu, Z. Mei, H. Chen, F. Pan, ACS Catal., 2018, 8, 5621-5629.

21. K. Dastafkan, Q. Meyer, X. Chen, C. Zhao, Small, 2020, 16, 2002412.

22. R. Li, B. Hu, T. Yu, H. Chen, Y. Wang, S. Song, Adv. Sci., 2020, 7, 1902830.

23. P. W. Menezes, C. Panda, S. Loos, F. Bunschei-Bruns, C. Walter, M. Schwarze, X. Deng, H. Dau, M. Driess, Energy Environ. Sci., 2018, 11, 1287-1298.

24. H. J. Song, H. Yoon, B. Ju, D. Y. Lee, D. W. Kim, ACS Catal., 2020, 10, 702-709.

25. L. Yang, H. Ren, Q. Liang, K.N. Dinh, R. Dangol, Q. Yan, Small, 2020, 16, 1906766.

26. M. Wang, C.L. Dong, Y.C. Huang, S. Shen, ACS Catal., 2020, 10, 1855-1864.

27. Y. Dou, C.T. He, L. Zhang, H. Yin, M. Al-Mamun, J. Ma, H. Zhao, Nat. Commun., 2020, 11, 1664.

28. Y. Xin, X. Kan, L.Y. Gan, Z. Zhang, ACS Nano, 2017, 11, 10303-10312.

29. Y. Wu, Y. Yi, Z. Sun, H. Sun, T. Guo, M. Zhang, L. Cui, K. Jiang, Y. Peng, J. Sun, Chem. Eng. J., 2020, 390, 124515.

30. E. Hu, Y. Feng, J. Nai, D. Zhao, Y. Hu, X. W. Lou, Energy Environ. Sci., 2018, 11, 872-880.

31. L. Yan, L. Cao, P. Dai, X. Gu, D. Liu, L. Li, Y. Wang, X. Zhao, Adv. Funct. Mater., 2017, 27, 1703455.

32. L. Chai, Z. Hu, X. Wang, Y. Xu, L. Zhang, T.T. Li, Y. Hu, J. Qian, S. Huang, Adv. Sci., 2020, 7, 1903195.

33. Y. Zhu, W. Zhou, Y. Zhong, Y. Bu, X. Chen, Q. Zhong, M. Liu, Z. Shao, Advanced Energy Mater., 2017, 7, 1602122. .

34. X. Gao, H. Zhang, Q. Li, X. Yu, Z. Hong, X. Zhang, C. Liang, Z. Lin, Angew. Chem. Int. Ed., 2016, 55, 6290-6294.

35. H. Liang, A.N. Gandi, D.H. Anjum, X. Wang, U. Schwingenschlögl, H.N. Alshareef, Nano Lett., 2016,16, 7718-7725.

36. L. Hang, T. Zhang, Y. Sun, D. Men, X. Lyu, Q. Zhang, W. Cai, Y. Li, J. Mater. Chem. A, 2018, 6, 19555-19562.

37. P. Kuang, M. He, H. Zou, J. Yu, K. Fan, Appl. Catal. B: Environ., 2019, 254, 15-25.

38. S. Dutta, A. Indra, Y. Feng, H. Han, T. Song, Appl. Catal. B: Environ., 2019, 241, 521-527.

39. R. Bose, V.R. Jothi, K. Karuppasamy, A. Alfantazi, S.C. Yi, J. Mater. Chem. A, 2020, 8, 13795-13805.

40. J. Lin, P. Wang, H. Wang, C. Li, X. Si, J. Qi, J. Cao, Z. Zhong, W. Fei, J. Feng, Adv. Sci., 2019, 6, 1900246.

41. Z. Dai, H. Geng, J. Wang, Y. Luo, B. Li, Y. Zong, J. Yang, Y. Guo, Y. Zheng, X. Wang, Q. Yan, ACS Nano, 2017, 11, 11031-11040.

42. Y. Li, B. Huang, Y. Sun, M. Luo, Y. Yang, Y. Qin, L. Wang, C. Li, F. Lv, W. Zhang, S. Guo, Small, 2019, 15, 1804212.

43. Y. Gong, Z. Yang, Y. Lin, J. Wang, H. Pan, Z. Xu, J. Mater. Chem. A, 2018, 6, 16950-16958.

44. L. Yang, R. Liu, L. Jiao, Adv. Funct. Mater., 2020, 30, 1909618.